Development and Characterization of a CMOS-MEMS Accelerometer With Differential LC-Tank Oscillators

Yi Chiu, Hao-Chiao Hong, *Senior Member, IEEE*, and Po-Chih Wu

***Abstract*— This paper presents a CMOS-MEMS accelerometer based on differential LC-tank oscillators. Two LC-tank oscillators composed of differential MEMS capacitors and suspended inductors were designed and fabricated by standard TSMC 0.18 μm CMOS processes and post-CMOS dry etching. The outputs of the differential oscillators are mixed and the output frequency of the mixer is proportional to the capacitance change caused by the external acceleration. The device has been characterized and has a mechanical resonance frequency of 7 kHz, absolute sensitivity of 3.62 MHz/g, relative sensitivity of 1.9 x 10^{-3} $\Delta f/f_0$/g, in-axis nonlinearity of 1.2 %FS, bias stability of 2.1 mg, and average noise floor of 0.205–0.219 mg/$\sqrt{}$Hz in the frequency range of 15–250 Hz. [2013-0134]**

***Index Terms*— Accelerometer, CMOS MEMS, differential capacitor, LC tank oscillator, frequency output, Allan's deviation.**

I. Introduction

ACCELEROMETERS are one of the most mature and widely used MEMS devices. They can be found in automobile airbags, navigation systems, digital cameras, mobile phones, and game controllers. The sensing mechanism of MEMS accelerometers can be capacitive, piezoresistive, or piezoelectric. Among the commonly used mechanisms, capacitive sensing has the advantage of high signal sensitivity, low temperature sensitivity, and good compatibility with IC or MEMS processes. Therefore, they can be easily fabricated with low cost and high reliability. It is also possible to integrate capacitive accelerometers with the mature CMOS integrated circuits on the same chip to further reduce the parasitic effects and improve sensor resolution.

Integrated CMOS-MEMS capacitive accelerometers have been widely studied [1]–[5]. In direct capacitance sensing, offset in circuits can cause saturation and reduce the dynamic range. Therefore, care must be taken to avoid the effects of offset or parasitics. For example, correlated double sampling [2] and chopper stabilization [3]–[5] are common circuit design to reduce the offset in amplifiers. In [3], a differential difference amplifier was further used to cancel the DC offset due to circuit mismatch. It is also possible to cancel the mismatch in sensing capacitors by using digitally controlled offset trimming capacitors as in [2] and [5]. In comparison, the functioning of the oscillation circuits in frequency-output sensors is less sensitive to circuit offset. Even though the oscillation frequency may vary from chip to chip due to process, voltage, and temperature (PVT) variations, it can be calibrated and will not affect the senor performance in practice.

Frequency output has the advantages of high sensitivity, high dynamic range, and less noise sensitivity. The output can be easily converted to digital codes by a counter without using complicated analog-to-digital converters (ADC). Moreover, sensor performance such as bandwidth and resolution can be tuned by changing the sampling frequency of the counter.

In frequency-output sensors, the measurand changes the oscillation frequency of the sensing oscillators. This sensing mechanism has been applied to a wide range of various sensors. For example, cantilever-based resonant sensors have been used to measure mass [6], [7], magnetic field [8], and viscosity [9]. In these mechanical resonant sensors, the resonant frequency is influenced by the change in the effective mass [6], [7], [9] or spring constant [8]. LC-tank oscillators have also been used to measure mass [7], acceleration [1], [10], magnetic beads with attached DNA [11], and intra-ocular pressure [12], [13] by variable capacitors [1], [7], [12], [13] or inductors [10], [11]. Other frequency-output sensors employed various forms of relaxation oscillators or ring oscillators to sense sound levels [14], touch [15], [16], DNA [17], humidity [18], light [19], and gas [20] by converting variations of capacitance [14]–[18], light intensity [19] or resistance [20] into oscillation frequency shift. Thermal dependence of the transistor characteristics such as propagation delay or threshold voltage can also be used to design frequency-output temperature sensors [21], [22].

For micro accelerometers, most of the demonstrated oscillator-based MEMS accelerometers with frequency output employed mechanical resonators such as double-ended tuning forks (DETF) [23]–[29], suspended mass-spring systems [30], or tuning forks [31], [32]. The resonant frequency of the mechanical resonators is usually between several kHz and several hundred kHz. Since the output frequency shift of the oscillators is proportional to the center oscillation frequency, the relatively low resonant frequency results in low

Manuscript received April 29, 2013; revised August 20, 2013; accepted September 15, 2013. Date of publication October 17, 2013; date of current version November 25, 2013. This work was supported by the National Science Council of Taiwan under Contract NSC 99-2220-E-009-027, Contract NSC 100-2221-E- 009-064, Contract NSC 101-2221-E-009-171, and Contract NSC 101-2623-E-009-009-D. Subject Editor A. J. Ricco.

The authors are with the Department of Electrical and Computer Engineering, National Chiao Tung University, Hsinchu 30013, Taiwan (e-mail: yichiu@mail.nctu.edu.tw; hchong@cn.nctu.edu.tw; roger22072862@hotmail.com).

Color versions of one or more of the figures in this paper are available online at http://ieeexplore.ieee.org.

Digital Object Identifier 10.1109/JMEMS.2013.2282419

1057-7157 © 2013 IEEE

absolute sensitivity which ranges up to a few hundred Hz/g in [23]–[32]. Thus long readout time is required if a counter is used to convert the frequency output to a digital code. The advantage of mechanical resonant accelerometers is that it can achieve high Q by vacuum packaging [23]–[32], which increases the manufacturing cost nonetheless, to improve the frequency stability and noise performance for inertial and navigation applications. However, it is still necessary to address the issue of proper damping of the shuttle mass for quick response in such a high-Q system. This has been demonstrated by using a more complex packaging [33] or structural design [32].

In contrast, LC-tank based oscillators can achieve higher oscillation frequency due to its non-mechanical nature and thus higher sensitivity can be obtained. For example, a center frequency of 2.1 GHz and a sensitivity of 10 kHz/g were reported in [10]. Even though LC oscillators have relatively low Q compared to mechanical oscillators, they can operate with sub-ppm frequency stability without vacuum packaging if carefully designed [11]. Even though the low-Q LC-oscillator-based accelerometers without vacuum packaging may not achieve the ultimate frequency stability of the high-Q mechanical-oscillator-based accelerometers packaged in vacuum, the former have the advantages of simpler processes and lower cost, simple and robust circuit architecture, large dynamic range, and digital output.

In this paper, an LC-oscillator-based CMOS-MEMS accelerometer targeted for industry, automobile, and consumer applications where mg-resolution is satisfactory is presented. Two LC-tank oscillators composed of comb-finger capacitors and suspended inductors were designed and fabricated by standard TSMC 0.18 μm CMOS processes and post-CMOS dry etching. The high oscillation frequency ($f_0 \approx 2$ GHz) enhances the absolute sensitivity compared to the traditional accelerometers employing direct capacitance sensing or mechanical resonators with low resonance frequency. The paper is structured as follows. Section II describes the operation principle of the proposed accelerometer and its MEMS and circuit design. Section III presents the fabricated devices and the characterization data. Both static and dynamic acceleration test data are presented and discussed. Some issues regarding the design and experimental observation are further discussed in Section IV. Finally, conclusion is given in Section IV.

II. Device Design

A. Operation Principle

In a capacitive MEMS accelerometer, the displacement of the shuttle mass caused by the external acceleration induces a change of the sensing capacitance C. In the proposed device, the sensing capacitance is connected with an inductor L to form a LC-tank resonator. The change of the sensing capacitance, ΔC, due to the acceleration induces a change of the oscillation frequency which can be read by a counter. As shown in Fig. 1, two LC-tank oscillators are designed with differential MEMS capacitors. The oscillation frequencies in the presence of the external acceleration are

$$f_{1,2} = 1/2\pi\sqrt{LC_{1,2}} = 1/(2\pi\sqrt{L(C_0 + C_{1p,2p} \pm \Delta C)}), \quad (1)$$

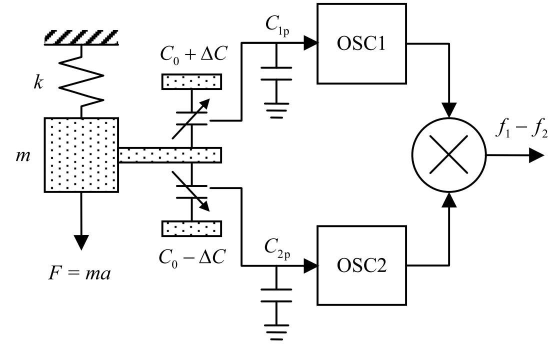

Fig. 1. Principle of the proposed MEMS LC-tank-based accelerometer.

where C_0 is the capacitance of the sensing fingers at rest and ΔC is the capacitance change caused by the acceleration. $C_{1p,2p}$ represents the loading capacitance, parasitic capacitance, and capacitance mismatch of the respective oscillators. The outputs of the two oscillators are mixed and down-converted to facilitate frequency counting. The mixed frequency after low-pass filtering is

$$f_1 - f_2 = (f_{10} - f_{20}) + \left(\frac{f_{10}}{2(C_0 + C_{1p})} + \frac{f_{20}}{2(C_0 + C_{2p})}\right)\Delta C, \quad (2)$$

where $f_{10,20} = 1/(2\pi L(C_0 + C_{1p,2p}))^{1/2}$ are the intrinsic oscillation frequencies without acceleration. The oscillators are implemented with $C_{1p} \neq C_{2p}$ so that the mixer output has a non-zero frequency bias $f_{10} - f_{20}$. This design avoids low output frequency and long sampling time for low acceleration and small ΔC. It also enables the distinction between negative and positive ΔC.

The frequency shift due to ΔC, i.e. the output signal, in the last term in (2) is proportional to the external acceleration as well as the center frequency $f_{10,20}$. Thus the absolute sensitivity (in Hz/g) of the sensor can be enhanced by using a high resonance frequency of the LC tanks. The large frequency shift due to the enhanced absolute sensitivity is desirable since it reduces the readout time to resolve different frequencies by the counter; therefore the signal bandwidth can be increased.

While the frequency shift Δf due to external acceleration can be enhanced by a large center frequency f_0, the relative frequency shift $\Delta f/f_0$ (in ppm $\Delta f/f_0$/g) is also important since it is related to the signal-to-noise ratio (SNR) and resolution. From (2), the relative sensitivity of one oscillator is $\Delta f/f_0 = \Delta C/2(C_0 + C_{1p})$. Therefore, the overall frequency sensitivity of the sensor is basically proportional to the capacitance sensitivity $\Delta C/(C_0 + C_p)$ determined by the mechanical and circuit design.

Whereas increasing the absolute sensitivity is needed for signal bandwidth, it is noted that the relative sensitivity in combination with frequency stability is what defines the accelerometer's in-run performance. Therefore the proposed LC-based accelerometer is attractive because of cost and is not to compete with the high-Q mechanical-resonator-based accelerometer which has good noise and bias performance.

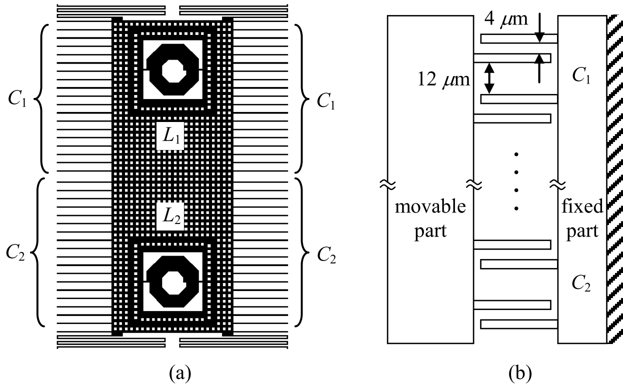

Fig. 2. (a) Schematic layout of the MEMS sensor (movable part), (b) asymmetric comb fingers.

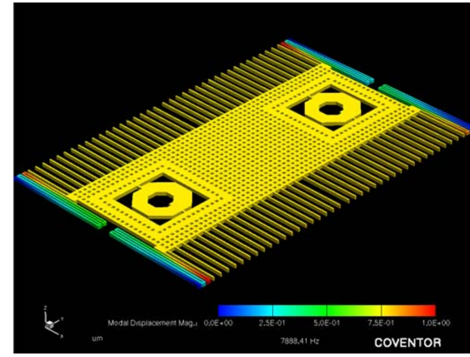

Fig. 3. First resonance mode of the MEMS structure.

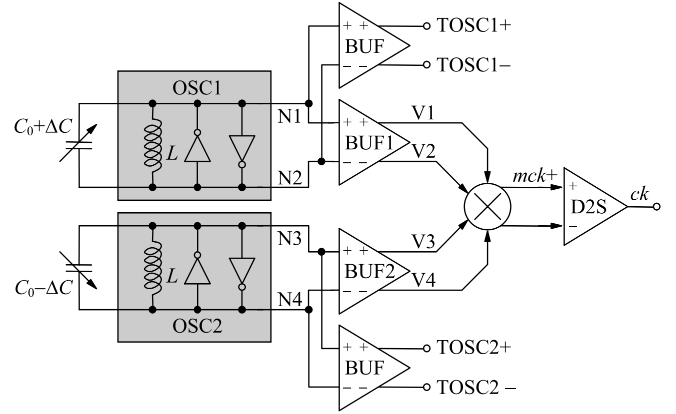

Fig. 4. Block diagram of the sensing circuit.

B. MEMS Sensor Design

The sensing capacitors are composed of typical MEMS parallel-plate capacitors between comb fingers; the inductors are integrated high-Q MEMS inductors embedded in the moving mass to improve the oscillator performance and reduce the chip size. The integrated inductor also eliminates the need for external inductors such as bonding wires [10] or package-level inductors [34] to further reduce the performance variation due to packaging.

The schematic layout of the MEMS sensor is shown in Fig. 2(a). It contains two sets of differential variable capacitors and two suspended inductors for the two LC-tank oscillators. The embedded spiral inductors are implemented in the M6 layer in the TSMC 0.18 μm 1P6M process. It has 5.5 turns and the metal width is 6 μm. The inductance and quality factor at 2 GHz are 4 nH and 6.6, respectively, calculated from the circuit model. The quality factor can be further improved by removing the substrate underneath it in the post-CMOS etching process [35], [36].

The capacitor fingers are composed of Poly1 to M6 stacks with via connecting the conductor layers. The thickness, width, and overlap length of the fingers are 10.15 μm, 4 μm, and 150 μm, respectively. According to the design rules of the post-CMOS dry-etching processes [35], [36], the minimum gap d between the fingers is 4 μm. Furthermore, the sensing fingers are designed with asymmetric gaps of 4 μm and 12 μm, as shown in Fig. 2(b), in order to distinguish the displacement in opposite directions. The capacitor for an oscillator has 38 pairs of comb fingers. The capacitance from the Coventorware simulation is 263 fF.

In the mass-spring model of the accelerometer, the sensitivity of a quasi-static accelerometer is

$$\Delta y/a_{\text{ext}} = 1/(2\pi f_0)^2, \tag{3}$$

where Δy is the displacement of the shuttle mass, a_{ext} is the external acceleration, and $f_0 = (k/m)^{1/2}/2\pi$ is the mechanical resonance frequency of the system. The four folded springs in Fig. 2(a) have a total spring constant k of 2.8 N/m. To design an accelerometer with $\Delta y/d = 1/1000$ and thus $\Delta C/C_0 = 1/1500$ in the asymmetric sensing capacitors at 1 g acceleration, it can be calculated from (3) that the accelerometer should have a resonance frequency f_0 of 7880 Hz and a mass m of 1.1×10^{-9} kg for the minimum finger gap of $d = 4$ μm. The Coventorware simulation shows the resonance frequencies of the first three modes are 7888 Hz (translation along the main sensing y axis) (Fig. 3), 9130 Hz (translation along the out-of-plane z axis), and 13090 Hz (rotation about the y axis). The translation in the y axis causes opposite change of the two sensing capacitance, as shown in Fig. 2(b), whereas the translation in the x or z directions causes the same change of the capacitance. Therefore, the cross sensitivity in the x and z directions in this differential sensing mechanism can be suppressed after the mixing takes the difference of the two oscillation frequencies even though the resonance frequencies of the first two modes are close to each other. The fixed fingers of the sensing capacitors are attached to a curled frame [37] to reduce the effect of residual stress. In the presence of a 1 g acceleration, the change of capacitance is about 0.2 fF in simulation.

C. Circuit Design

The block diagram of the sensing circuit is shown in Fig. 4. It consists of two differential oscillators controlled by the differential MEMS sensing capacitors, two buffers BUF1 and BUF2 to isolate the kick-back noise from the backend stages, a Gilbert cell for mixing the outputs of the oscillators, and a differential-to-single-ended converter (D2S) for generating the rail-to-rail clock output ck. An external counter can be used to count the rising edges of ck within a sampling period $1/f_s$

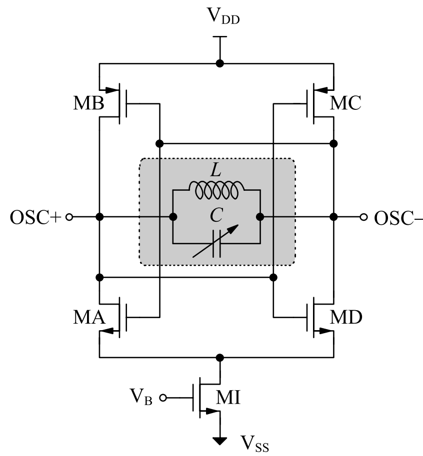

Fig. 5. Schematic of the LC-tank oscillator.

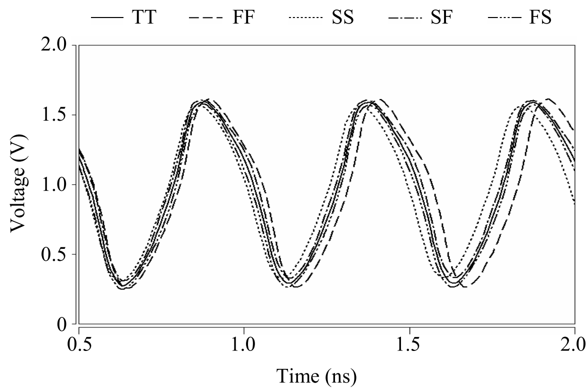

Fig. 6. Simulation results of the LC-tank oscillator for various process corners.

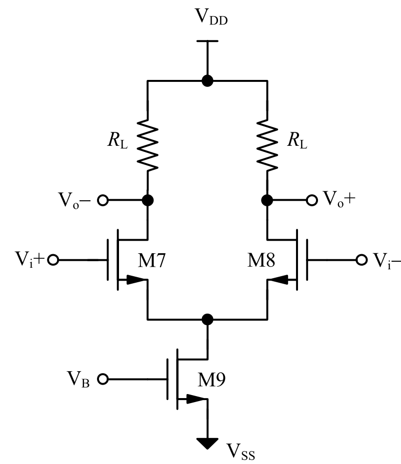

Fig. 7. Schematic of the buffer.

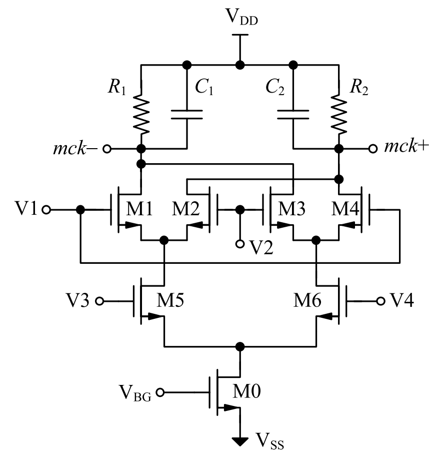

Fig. 8. Schematic of the Gilbert cell.

and output the digital code. For testing purposes, two buffers BUF are added at the outputs of the oscillators to observe the raw oscillation signals.

The schematic of the fully differential LC-tank oscillator is shown in Fig. 5 where the inductor and the capacitor are fabricated by CMOS-MEMS technology. The equivalent negative resistance -1/g_m of the active transistors is used to compensate for the power loss due to the parasitic resistance R_s of the inductor and the capacitor. To sustain stable oscillation, it is required that $g_m > 1/R_s$. After the RC extraction of R_s in the layout, the required transconductance g_m can be obtained by the adjusting the tail current through MI. Fig. 6 shows the simulation results of the oscillator OSC1 for various process corners. As explained in Section II.A, increasing the oscillation frequency can enhance the sensitivity of the accelerometer. However, the oscillation frequency of practical oscillators in 0.18 μm processes is around 2–5 GHz due to process limits. Therefore, the oscillation frequencies of the two oscillators OSC1 and OSC2 are designed to be about 2.0 GHz and 1.9 GHz, respectively.

The outputs of the two oscillators go to two buffers for amplification and common-mode level adjustment before they are mixed since the two input pairs of the mixer need different bias voltages to function properly. All buffers have the same design as shown in Fig. 7 except for different loading resistors for adjusting the common-mode output levels and thus the bias of M7 and M8. It is noted that the different bias conditions of M7/M8 intrinsically introduce a difference in the parasitic capacitance C_{1p} and C_{2p} at nodes N1/N2 and N3/N4 in Fig. 4 for the frequency bias $f_{10} - f_{20}$, according to (1) and (2).

A Gilbert cell, as shown in Fig. 8, is used to mix the amplified oscillator signals. The buffered oscillator signals are connected to the V1/V2 and V3/V4 terminals, respectively. The two differential inputs are biased at different levels to keep all transistors of the Gilbert cell operating in the saturation mode. The mixed signal has two frequency components $f_1 \pm f_2$. C_1 and C_2 in the circuits are used to filter out the high-frequency component. In the present design, the resistance and capacitance of the RC filter are 5 kΩ and 50 fF, respectively. With additional parasitic capacitance of 30 fF, the pole of the filter is at about 400 MHz for the signal frequency at 100 MHz. Since the ratio of the two frequency components is about 40, the simple RC low-pass filter can provide 32-dB attenuation for the high-frequency component. The intrinsic bandwidth of the Gilbert cell and the parasitic resistance and capacitance of the routing wires provide additional attenuation.

The differential output of the Gilbert cell goes through a differential-to-single-ended converter to generate the rail-to-

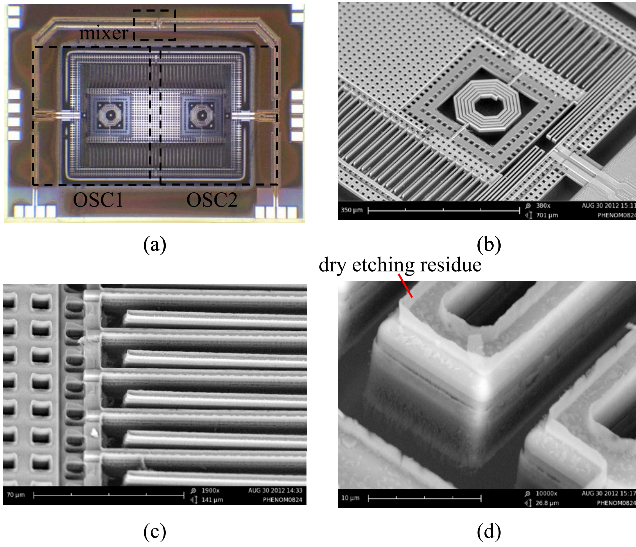

Fig. 9. (a) Photograph and (b) SEM microgram of a released chip, (c) comb fingers, (d) spring.

rail output signal *ck* before it is observed by oscilloscopes or spectrum analyzers. The output frequency variation can be converted to a digital code by a simple counter without the high-resolution and complex ADC used in conventional accelerometers [38]–[40]. For example, the proposed accelerometer with a counter operating at a sampling rate f_s of 500 Hz can achieve a digital output code with more than 17-bit resolution. The ADC with such a resolution is much more difficult to design and the hardware cost is much higher than the counter.

III. Experiments

A. Post Processing

The proposed CMOS-MEMS accelerometer was first fabricated by the standard TSMC 0.18 μm CMOS processes through the service of the Chip Implementation Center (CIC), Taiwan. After the CMOS processes, the post processing offered by the CIC was adopted to release the structure. An additional photoresist layer was first coated and patterned as the etching mask for structure release. Anisotropic SiO_2 dry etching was used to define the MEMS structures such as fingers, springs, and mass. Isotropic Si dry etching was then used to remove the silicon substrate and release the structure [35], [36]. Fig. 9 shows the images of a released device.

In addition to defining the mechanical structures, the photoresist layer in the post-CMOS processes also offers additional protection of the circuits and structures against the ion bombardment during dry etching. It was shown in [36] that circuit drift was insignificant in a 5.8 GHz low noise amplifier fabricated by the same CMOS and post-CMOS processes as used in this paper. Therefore, all circuit regions in this paper were covered by the photoresist in the post-CMOS processes.

B. Mechanical Measurement

The measured mechanical resonance frequency and quality factor Q in atmospheric environment are about 7 kHz and 17, respectively, as shown in Fig. 10. The Brownian noise equivalent acceleration (BNEA) can be calculated as

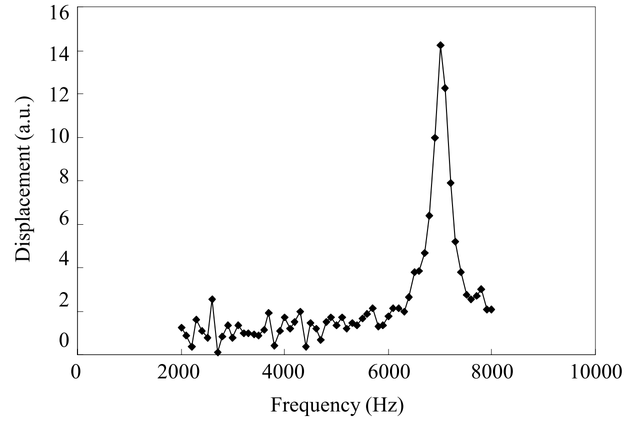

Fig. 10. Measured mechanical frequency response of the sensor.

$$\mathrm{BNEA} = \sqrt{4k_B T\omega_0/Qm} = 20\ \mu\mathrm{g}/\sqrt{\mathrm{Hz}}. \quad (4)$$

The possible causes of the slight discrepancy between measured and expected resonance frequencies include (1) variation in material properties such as Young's modulus and residual stress, (2) variation in geometry such as the thickness of various metal and dielectric layers in the CMOS processes, and (3) variation in geometry due to post-CMOS processing such as the attack and residuals of the dry etching. At this moment, no data regarding these variations are available for mechanical corner simulation. Therefore, it is important to follow the CMOS and the post-CMOS design rules provided by the foundry services to ensure consistent performance. Nevertheless, a process variation of about 10% is reasonable from published documents.

C. Static Acceleration Measurement

The sensor response to static acceleration was characterized in the tumble test by mounting the device on a rotation table with an angular accuracy of $\pm 1°$. The local gravity was used as the input acceleration. The output oscillation frequency f can be modeled as a function of the in-axis acceleration component a_y and the cross-axis acceleration component a_x,

$$\begin{aligned} f &= f(a_y, a_x) \\ &= f_0 + S_y a_y + S_x a_x + S_{yy} a_y^2 + S_{xy} a_x a_y, \end{aligned} \quad (5)$$

where f_0 is the bias frequency, S_x is the in-axis sensitivity (or scale factor), S_y is the linear cross-axis sensitivity, S_{yy} is the second order nonlinearity, and S_{xy} is the second-order cross coupling. In the tumble test, $a_y = \cos\theta$ and $a_x = \sin\theta$; equation (5) can be re-written as

$$f = f_0 + S_y \cos\theta + S_x \sin\theta + S_{yy}\cos^2\theta + S_{xy}\cos\theta\sin\theta. \quad (6)$$

It is noted that the linear cross-axis sensitivity can also be caused by an angular misalignment and there is no way of distinguishing between the two. Nevertheless, the coefficient S_x will be referred to as the cross-axis sensitivity in the following discussion, as in most literatures, even though angular misalignment is used in [41].

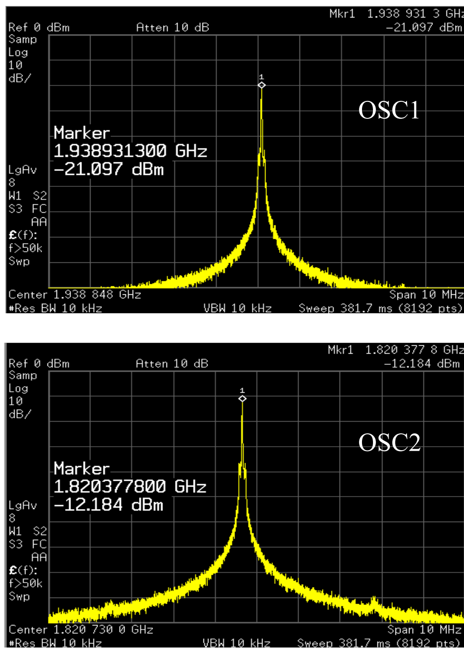

Fig. 11. Measured spectra of the oscillators in static conditions.

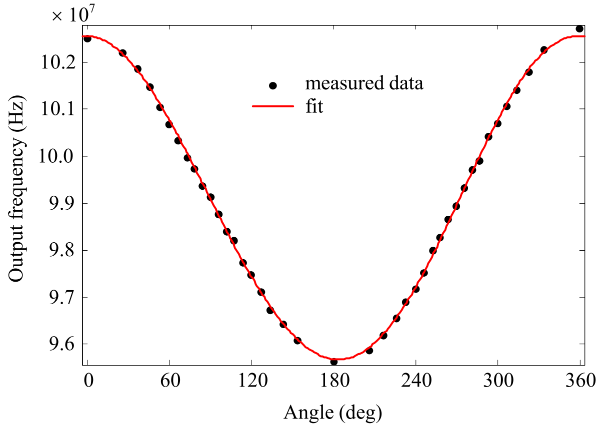

Fig. 12. Static tumble test.

Fig. 11 shows the output spectra of the oscillators in a typical device measured by an Agilent 4440A spectrum analyzer in static test conditions. The measured oscillation frequencies of the two oscillators are 1.939 GHz and 1.820 GHz, respectively, indicating a frequency bias $f_{10} - f_{20}$ of about 100 MHz at the mixer output. The phase noise of a typical oscillator is-114 dBc/Hz at 1 MHz offset, which is comparable to a 5.8 GHz voltage-controlled oscillator fabricated by the same CMOS and post-CMOS processes [35]. Fig. 12 shows the measured static output frequency vs. rotation angle. The data are fit to the following model equation [41]

$$f = a_0 + a_1 \cos\theta + a_2 \cos 2\theta + b_1 \sin\theta + b_2 \sin 2\theta \quad (7)$$

and the coefficients in (6) can be found from the Fourier

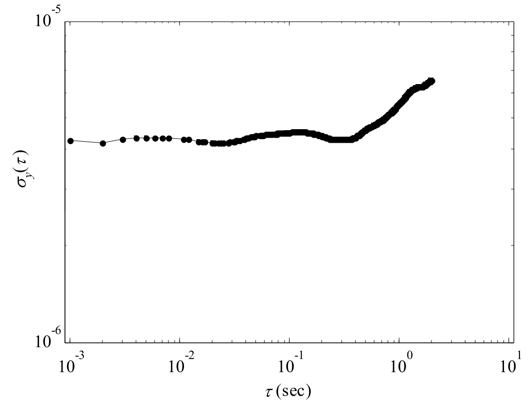

Fig. 13. Allan's deviation of the fractional frequency.

coefficients in (7),

$$\begin{aligned} f_0 &= a_0 - a_2 = 9.90 \times 10^7 \text{ Hz}, \\ S_y &= a_1 = 3.44 \times 10^6 \text{ Hz/g}, \\ S_x &= b_1 = 6.34 \times 10^4 \text{ Hz/g}, \\ S_{yy} &= 2a_2 = 5.44 \times 10^4 \text{ Hz/g}^2, \\ S_{xy} &= 2b_2 = -1.32 \times 10^5 \text{ Hz/g}^2. \end{aligned} \quad (8)$$

From the above coefficients, the linear cross-axis sensitivity is $S_x/S_y = 1.8\%$ and the in-axis nonlinearity is $S_{yy}/S_y = 1.58$ %FS for ± 1 g input.

The frequency stability of the oscillator was characterized by the Allan's deviation [42] while the sensor was at rest. The output frequency was measured by a Standford Research SR 620 frequency counter at a sampling rate of 1 kHz. The Allan's deviation of the fractional frequency with respect to the nominal 1.9 GHz oscillation frequency was calculated from the measured data by a Matlab code [43]. As shown in Fig. 13, the frequency stability is about 4 ppm (corresponding to an accelerometer bias stability of 2.1 mg) and remains relatively constant for the average time τ from 1 ms to 0.3 sec. This τ^0 dependence indicates the dominant noise is the frequency flicker noise [42], which can also be observed on the spectrum of the measured frequency. For longer average time, the deviation has a $\tau^{1/2}$ dependence due to frequency random walk [42] which was probably caused by the poor control of temperature and EMI in the testing environment. As shown in Fig. 9(a), the two oscillator circuits are physically distant from each other. The post processes and residual stress may also cause structural asymmetry in the released device. These factors reduce the common-mode rejection of the environmental variation in the sensor output. Therefore, the frequency stability can be improved by a more careful circuit design, as in [11], or mechanical design, as in [32], for better temperature compensation. The flicker noise can be reduced by properly adjusting the transistor sizes in the current design.

D. Dynamic Acceleration Measurement

The sensor was excited by an electromagnetic shaker (LDS V406) in the main sensing direction with excitation

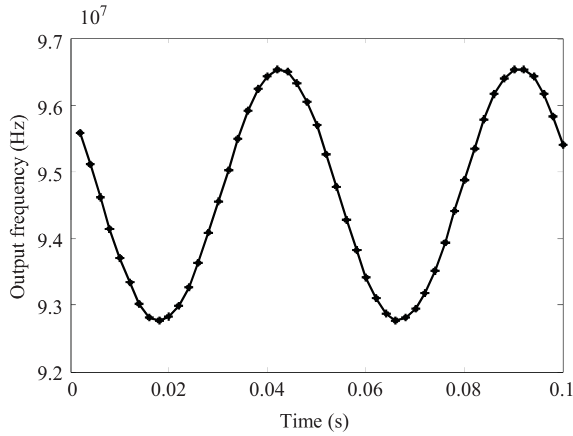

(a)

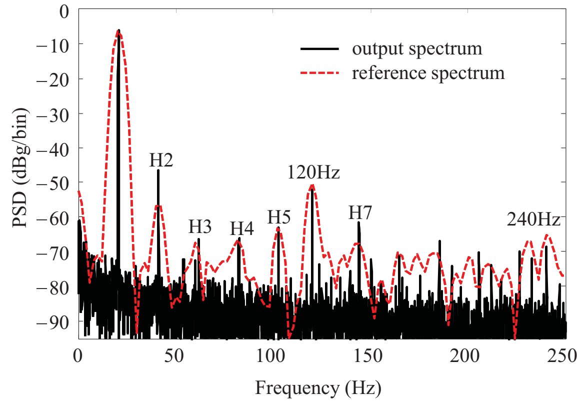

(b)

Fig. 14. Dynamic acceleration test, (a) sensor output signal, (b) spectra of the sensor output and the reference output showing power noise and harmonics.

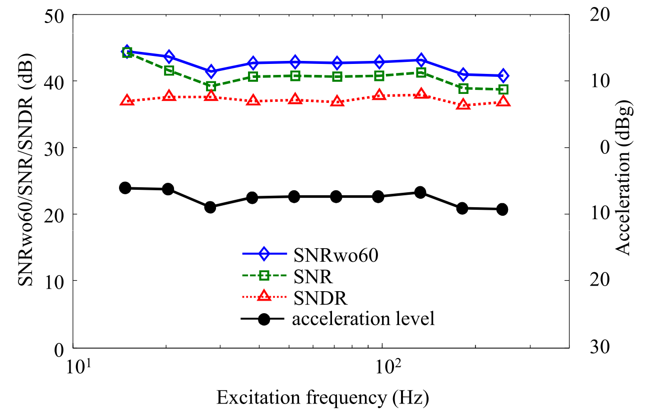

(a)

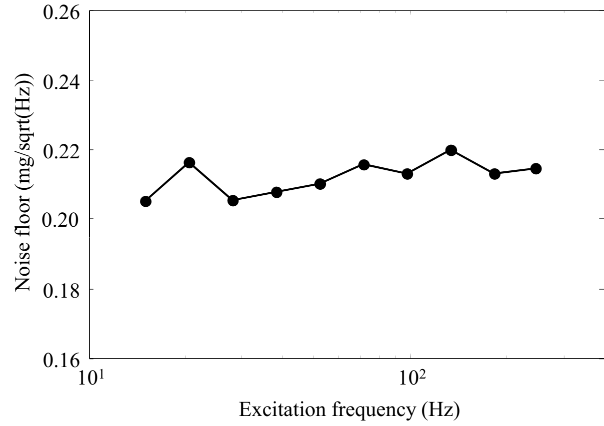

(b)

Fig. 15. (a) Frequency response test, (b) measured average noise floor.

frequency f_{in}. A commercial accelerometer (PCB Piezotronics model 353B17) was used as a reference to determine the excitation level a_{ext}. The output frequency was measured by the frequency counter with a sampling frequency f_s. After the time trace of the output was recorded, its spectrum was calculated by fast Fourier transform (FFT) to decide the output signal level and the signal-to-noise ratio (SNR).

Fig. 14 shows the output signal and its spectrum of a typical measurement with $f_{\text{in}} = 20.54$ Hz, $f_s = 500$ Hz, and nominal acceleration amplitude $a_{\text{ext}} = 0.5$ g. The data show that the sensor in the test achieves a SNR of 41.5 dB and a signal-to-noise-and-distortion ratio (SNDR) of 37.7 dB. It corresponds to an average noise floor in the measurement bandwidth of

$$a_{\text{ext}} 10^{-\text{SNR}/20} / \sqrt{f_s/2} = 0.276 \text{ mg}/\sqrt{\text{Hz}}. \quad (9)$$

Fig. 14(b) indicates the second harmonic (H2) and the 120 Hz AC power noise are the dominant components that deteriorate the SNDR performance of the sensor. To determine the root causes that limit the sensor noise floor, the measured spectrum of the reference accelerometer is also plotted in Fig. 14(b). It can be seen that the shaker contains significant harmonic signals (H2 to H7). However, the sensor output has a relatively higher second harmonic caused by the stress-induced curling sensing fingers and thus nonlinearity in the transfer characteristics. Fig. 14(b) also indicates the most significant noise components are the AC power noises at 120 Hz and 240 Hz; they are introduced by the shaker because they appear in all dynamic tests but not in static tests. These AC power noises should not be considered as a part of the sensor noise. To exclude the power noise, we define SNRwo60 as the SNR without the 60-Hz noise and its harmonics. This value represents a better evaluation of the actual sensor characteristics. The SNRwo60 value of the sensor output in Fig. 14(b) is 43.7 dB, corresponding to an average noise floor of

$$a_{\text{ext}} 10^{-\text{SNRwo60}/20} / \sqrt{f_s/2} = 0.216 \text{ mg}/\sqrt{\text{Hz}}. \quad (10)$$

Fig. 15(a) shows the measured SNDR, SNR, and SNRwo60 for various excitation frequency f_{in} at $f_s = 500$ Hz and the same nominal excitation amplitude $a_{\text{ext}} = 0.5$ g (-6 dBg). The SNR and SNRwo60 results are between 44.2 dB to 38.7 dB and 44.3 dB to 40.7 dB, respectively. Fig. 15(a) also plots the acceleration levels calculated from the signal tone in the measured data. The acceleration levels vary from -6 to -9.2 dBg though their nominal values are -6 dBg as observed from the time-domain output of the reference accelerometer. This explains the fluctuation of the SNR/SNRwo60 plots. It also implies that the harmonic distortion of the shaker varies from measurement to measurement.

Fig. 15(b) depicts the average noise floor in the measurement bandwidth vs. the acceleration frequency. Since the SNR values are limited by the 120Hz and 240Hz AC power noises,

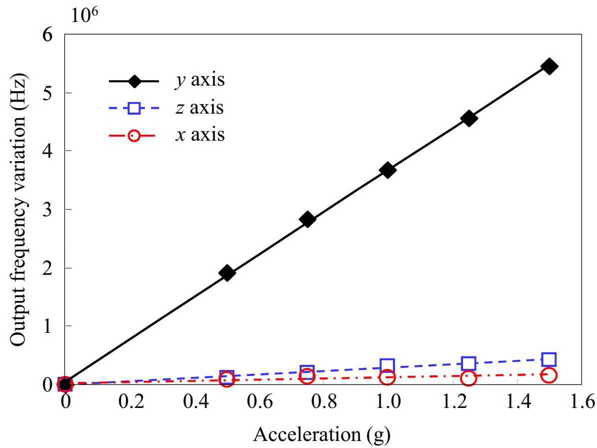

Fig. 16. Output signal vs. input acceleration.

TABLE I
SENSITIVITY AND NONLINEARITY SUMMARY

Axis	Sensitivity (MHz/g)	% y axis
y	3.62	-
z	0.29	8.1
x	0.08	2.3

the SNRwo60 values are used to compute the noise floor. The measured average noise floor is within a narrow range of 0.205 to 0.219 mg/$\sqrt{}$Hz, showing the tests have very consistent noise power in the excitation frequency range of 15 to 250 Hz. For systems with bandwidth of 10−1000 Hz such as the targeted consumer, automobile, and industrial applications, the corresponding resolution of the accelerometer is about 0.66–6.6 mg.

Fig. 16 shows the output levels with respect to the input acceleration levels at $f_{in} = 20.54$ Hz and $f_s = 500$ Hz. The calculated absolute sensitivity, relative sensitivity, and nonlinearity in the main sensing axis (y) are 3.62 MHz/g, 1.9×10^{-3} $\Delta f/f_0$/g, and 1.2 %FS, respectively, which match well with the static measurement results. Cross-axis sensitivity was also measured by position the sensor along different directions in the dynamic tests. The results are summarized in Table I. The x axis has a 2.3% cross-axis sensitivity, close to the static measurement results. The z axis has a relatively high cross-axis sensitivity of 8.1% caused in part by the similar mechanical resonance frequency and in part by the non-uniform deformation due to residual stress after the proof mass was released. These testing results show that the demonstrated accelerometer achieved a much higher absolute sensitivity for sensor bandwidth, comparable relative sensitivity, and comparable noise floor compared with the state-of-the-art works, as shown in Table II.

IV. DISCUSSION

A number of issues regarding the design and experimental observation are discussed in the following in order to gain more insight to the device characteristics.

A. Bias Frequency

The choice of the frequency difference of the two oscillators, and thus the bias of the output frequency, is a trade-off of a number of factors. Increasing the bias frequency can increase the input dynamic range, reduce the readout time of the frequency counting, and increase the input bandwidth. However, larger frequency bias will require a counter with more bits and thus more chip area, induce a more asymmetric circuit architecture and thus less common-mode interference rejection, and reduce the overall sensitivity if it is realized by reducing the frequency of one of the oscillators, according to (2). In this paper, a bias frequency of 100 MHz was used as a typical digital design to demonstrate the functionality of the sensor.

B. Sensitivity

From (1) and (2), the frequency sensitivity of the oscillator is proportional to $f_0/(C_0 + C_p)$, which is in turn proportional to f_0^3 if the inductance is kept constant. The 5% difference between the two oscillation frequencies (2.0 vs. 1.9 GHz in design or 1.9 vs. 1.8 Hz in observation) implies a 15% difference in sensitivity of the respective oscillators. Therefore the two oscillators contribute almost equally to the overall sensitivity.

The oscillation frequency f_0 is determined by the MEMS capacitance C_0, MEMS inductance L, as well as the parasitic capacitance C_p at nodes N1/N2 and N3/N4, according to (1). The parasitic capacitance includes the gate capacitance of the transistors (MA to MD) in the oscillator, the input capacitance of the following buffer, and the parasitic capacitance of the routing wires. The 2-GHz oscillation frequency in the post-layout simulation agrees well with the measured result at 1.9 GHz. Accordingly, the parasitic capacitance is about 1.31 pF for $C_0 = 263$ fF, $L = 4$ nH, and $f_0 = 2$ GHz. The degradation of the sensitivity due to the large parasitic capacitance in the circuit can be calculated as follows. The MEMS capacitance was designed with a sensitivity of $\Delta C/C_0 = 1/1500$ per g, as discussed in Sec. II B. Therefore the theoretical overall sensitivity is

$$\Delta f = f_0 \frac{\Delta C}{C_0 + C_p} = f_0 \frac{C_0}{C_0 + C_p} \frac{\Delta C}{C_0} = 220 \text{ kHz/g}. \quad (11)$$

This value is very small compared to the measured sensitivity around 3.5 MHz/g obtained by different instruments (spectrum analyzers and counters) and in different test conditions (static vs. dynamic). While a quantitative analysis is still being investigated, the possible reasons for this discrepancy include

1) parasitic inductance of the wires in the spring and its additional sensitivity to the acceleration;
2) structural damage/variation of the spring or mass that changes the mechanical response to the acceleration.

C. Effect of Magnetic Field on Sensor Performance

In some cases the magnetic field such as that from the shaker may interfere with the sensor test, especially when

TABLE II
PERFORMANCE COMPARISON OF OSCILLATOR-BASED ACCELEROMETERS

Reference	[10]	[23]	[24]	[25]	[26]	[27]	[28]	[29]	[30]	[32]	This work
IC technology	0.13 μm	3 μm	2 μm	-	0.18 μm	-	-	0.15 μm	-	-	0.18 μm
MEMS technology	-	BiMOS2C	pre-CMOS	-	SOIMUMPs	-	ThELMA	ThELMA	-	SOI	post-CMOS
Integration	monolithic	monolithic	monolithic	-	two-chip	-	-	WLP	-	-	monolithic
Test in vacuum	no	yes	yes	yes	yes	yes	yes	yes	yes	yes	no
f_M [1]	3.1 kHz (Au) 8.7 kHz (Al)	-	-	-	-	-	-	-	-	-	7 kHz
f_0 [2] (resonator) [3]	2.1 GHz (elec LC)	175 kHz (mech)	145 kHz (mech)	28.4 kHz (mech)	128 kHz [4] (mech)	890 kHz (mech)	58 kHz (mech)	78.05 kHz (mech)	5.7 kHz (mech)	2.6 kHz (mech)	1.9 GHz (elec LC)
Mechanical quality factor Q	100 [4]	72000	10000	200	30000	5090	200	-	29274	30000 [6]	17
Absolute sensitivity (/g)	10 kHz	2.4 Hz	17 Hz	128 Hz	75 Hz [4]	3.4 Hz	455 Hz	256 Hz	24.7 Hz	4.4 Hz	3.62 MHz
Relative sensitivity (ppm $\Delta f/f_0$/g)	4.8	13.7	117	4500	590	3.8	8800	3300	4300	1700	1900
Noise floor (/$\sqrt{\text{Hz}}$) (test frequency, Hz)	80 mg [5]	15.8 mg [5]	40 μg (300)	5.2 μg [5]	20 μg [5]	0.9 mg (10-200)	0.46 mg [5]	0.36 mg [5]	-	25 μg [5]	0.205-0.219 mg (15-250)
Non-linearity	-	-	-	-	-	-	-	-	< 2%		1.2%
Cross-axis sensitivity	8% [4]	-	-	-	-	-	-	-	-		2.3% 8.1%

[1] mechanical resonance frequency [2] oscillator frequency (average) [3] electrical LC or mechanical resonators [4] estimated from figures
[5] obtained from Allan's deviation measurement [6] predicted by simulation

there are magnetic materials or components (e.g. inductors) in the sensors. We have measured the magnetic field from the shaker at the location where the sensors were placed. The DC component is about 1 mT and the AC component at all test frequency is below 0.01 mT (limited by the F. W. Bell model 5180 Gauss meter). The first possibility of the shaker magnetic field interfering with the sensor is the Lorentz force due to the current in the movable structure. Since there is no DC current in the movable structure which contains only the inductors and the capacitors for the oscillators, the Lorentz force at the vibration frequency due to the AC magnetic field is negligible. The force due to the DC field and the AC current in the structure is at the 1.9 GHz oscillation frequency, which is far beyond the mechanical bandwidth. Therefore it can also be neglected. However, the vibrating inductor in the magnetic field may induce an electromotive force (EMF) due to the time-varying magnetic flux. This EMF may introduce a low-frequency bias variation of the oscillator circuits and affect the measurement results. Further theoretical and experimental work is needed to investigate this issue.

V. CONCLUSION

A CMOS-MEMS accelerometer based on differential LC-tank oscillators is proposed and demonstrated. Two LC-tank oscillators composed of differential MEMS capacitors and suspended inductors were designed and fabricated by standard TSMC 0.18 μm CMOS processes and post-CMOS dry etching. The inductor is embedded in the moving mass to reduce the chip area. The high oscillation frequency of the LC-tank oscillators enhances the absolute sensitivity of the proposed accelerometer. The fabricated device has a mechanical resonance of 7 kHz. The measured absolute sensitivity, relative sensitivity, and nonlinearity of the accelerometer are 3.62 MHz/g, 1.9×10^{-3} $\Delta f/f_0$/g, and nonlinearity of 1.2 %FS, respectively. The accelerometer has a bias stability of 2.1 mg. The average noise floor measured between 15 and 250 Hz is 0.205–0.219 mg/$\sqrt{\text{Hz}}$. Deviation of device dimensions and performance due to post processing and measurement will be investigated and improved in the future. The proposed device is attractive for low-cost industrial, automobile, and consumer applications, whereas vacuum-packaged mechanical-resonator-based accelerometers would be needed for high-end navigation-grade applications due to their better noise and bias stability performance.

ACKNOWLEDGMENT

The authors were grateful to the use of facilities at the Chip Implementation Center, the National Center for High-performance Computing, the National Nano Device Laboratory, and the National Chiao Tung University Nano Facility Center, Taiwan.

REFERENCES

[1] Y. Chiu, H.-C. Hong, and P.-C. Wu, "CMOS-MEMS accelerometer with differential LC-tank oscillators," in *Proc. IEEE Sensors*, Oct. 2012, pp. 166–169.

[2] M. Lemkin and B. E. Boser, "A three-axis micromachined accelerometer with a CMOS position-sense interface and digital offset-trim electronics," *IEEE J. Solid-State Circuits*, vol. 34, no. 4, pp. 456–468, Apr. 1999.

[3] J. Wu, G. K. Fedder, and L. R. Carley, "A low-noise low-offset capacitive sensing amplifier for a 50-μg/$\sqrt{\text{Hz}}$ monolithic CMOS MEMS accelerometer," *IEEE J. Solid-State Circuits*, vol. 39, no. 5, pp. 722–730, May 2004.

[4] C.-M. Sun, M.-H. Tsai, Y.-C. Liu, and W. Fang, "Implementation of a monolithic single proof-mass tri-axis accelerometer using CMOS-MEMS technique," *IEEE Trans. Electron Devices*, vol. 57, no. 7, pp. 1670–1679, Jul. 2010.

[5] S.-S. Tan, C.-Y. Liu, L.-K. Yeh, Y.-H. Chiu, M. S. Lu, and K. Y.-J. Hsu, "An integrated low-noise sensing circuit with efficient bias stabilization for CMOS MEMS capacitive accelerometers," *IEEE Trans. Circuits Syst. I, Reg. Papers*, vol. 58, no. 11, pp. 2661–2672, Nov. 2011.

[6] D. Lange, C. Hagleitner, A. Hierlemann, O. Brand, and H. Baltes, "Complementary metal oxide semiconductor cantilever arrays on a single chip: Mass-sensitive detection of volatile organic compounds," *Anal. Chem.*, vol. 74, no. 13, pp. 3084–3095, Jul. 2002.

[7] S.-J. Kim, T. Ono, and M. Esashi, "Capacitive resonant mass sensor with frequency demodulation detection based on resonant circuit," *Appl. Phys. Lett.*, vol. 88, no. 5, pp. 053116-1–053116-3, Jan. 2006.

[8] R. Sunier, T. Vancura, Y. Li, K.-U. Kirstein, H. Baltes, and O. Brand, "Resonant magnetic field sensor with frequency output," *J. Microelectromech. Syst.*, vol. 15, no. 5, pp. 1098–1107, Oct. 2006.

[9] A. Agoston, F. Keplinger, and B. Jakoby, "Evaluation of a vibrating micromachined cantilever sensor for measuring the viscosity of complex organic liquids," *Sens. Actuators A, Phys.*, vols. 123–124, pp. 82–86, Sep. 2005.

[10] Y.-T. Liao, W. J. Biederman, and B. P. Otis, "A fully integrated CMOS accelerometer using bondwire inertial sensing," *IEEE Sensors J.*, vol. 11, no. 1, pp. 114–122, Jan. 2011.

[11] H. Wang, Y. Chen, A. Hassibi, A. Scherer, and A. Hajimiri, "A frequency-shift CMOS magnetic biosensor array with single-bead sensitivity and no external magnet," in *ISSCC Dig. Tech. Papers*, Feb. 2009, pp. 438–440.

[12] J. Coosemans, M. Catrysse, and R. Puers, "A readout circuit for an intra-ocular pressure sensor," *Sens. Actuators A, Phys.*, vol. 110, nos. 1–3, pp. 432–438, Feb. 2004.

[13] P.-J. Chen, S. Saati, R. Varma, M. S. Humayun, and Y.-C. Tai, "Wireless intraocular pressure sensing using microfabricated minimally invasive flexible-coiled lc sensor implant," *J. Microelectromech. Syst.*, vol. 19, no. 4, pp. 721–734, Aug. 2010.

[14] M. Pedersen, W. Olthuis, and P. Bergveld, "An integrated silicon capacitive microphone with frequency-modulated digital output," *Sens. Actuators A, Phys.*, vol. 69, no. 3, pp. 267–275, Sep. 1998.

[15] S. Guo, J. Guo, and W. H. Ko, "A monolithically integrated surface micromachined touch mode capacitive pressure sensor," *Sens. Actuators A, Phys.*, vol. 80, no. 3, pp. 224–232, Mar. 2000.

[16] C.-T. Ko, S.-H. Tseng, and M. S.-C. Lu, "A CMOS micromachined capacitive tactile sensor with high-frequency output," *J. Microelectromech. Syst.*, vol. 15, no. 6, pp. 1708–1714, Dec. 2006.

[17] C. Stagni, C. Guiducci, L. Benini, B. Riccò, S. Carrara, B. Samorí, C. Paulus, M. Schienle, M. Augustyniak, and R. Thewes, "CMOS DNA sensor array with integrated A/D conversion based on label-free capacitance measurement," *IEEE J. Solid-State Circuits*, vol. 41, no. 12, pp. 2956–2964, Dec. 2006.

[18] C.-L. Dai, "A capacitive humidity sensor integrated with micro heater and ring oscillator circuit fabricated by CMOS-MEMS technique," *Sens. Actuators B, Chem.*, vol. 122, no. 2, pp. 375–380, Mar. 2007.

[19] X. Wang, W. Wong, and R. Hornsey, "A high dynamic range CMOS image sensor with inpixel light-to-frequency conversion," *IEEE Trans. Electron Devices*, vol. 53, no. 12, pp. 1543–1554, Dec. 2006.

[20] M. Grassi, P. Malcovati, and A. Baschirotto, "A 141-dB dynamic range CMOS gas-sensor interface circuit without calibration with 16-bit digital output word," *IEEE J. Solid-State Circuits*, vol. 42, no. 7, pp. 1543–1554, Jul. 2007.

[21] P. Chen, C.-C. Chen, C.-C. Tsai, and W.-F. Lu, "A time-to-digital-converter-based CMOS smart temperature sensor," *IEEE J. Solid-State Circuits*, vol. 40, no. 8, pp. 1642–1648, Aug. 2005.

[22] F. Kocer and M. P. Flynn, "An RF-powered, wireless CMOS temperature sensor," *IEEE Sensors J.*, vol. 6, no. 3, pp. 557–564, Jun. 2006.

[23] T. A. Roessig, R. T. Howe, A. P. Pisano, and J. H. Smith, "Surface-micromachined resonant accelerometer," in *Proc. Int. Conf. Solid State Sensors Actuat.*, Jun. 1997, pp. 859–862.

[24] A. A. Seshia, M. Palaniapan, T. A. Roessig, R. T. Howe, R. W. Gooch, T. R. Schimert, and S. Montague, "A vacuum packaged surface micromachined resonant accelerometer," *J. Microelectromech. Syst.*, vol. 11, no. 6, pp. 784–792, Dec. 2002.

[25] S. Seok, H. Kim, and K. Chun, "An inertial-grade laterally-driven MEMS differential resonant accelerometer," in *Proc. IEEE Sensors*, Oct. 2004, pp. 654–657.

[26] L. He, Y.-P. Xu, and M. Palaniapan, "A CMOS readout circuit for SOI resonant accelerometer with 4-μg bias stability and 20 $\mu g/\sqrt{\mathrm{Hz}}$ resolution," *IEEE J. Solid-State Circuits*, vol. 43, no. 6, pp. 1480–1490, Jun. 2008.

[27] R. H. Olsson, K. E. Wojciechowski, M. S. Bake, M. R. Tuck, and J. G. Fleming, "Post-CMOS-compatible aluminum nitride resonant MEMS accelerometers," *J. Microelectromech. Syst.*, vol. 18, no. 3, pp. 671–678, Jun. 2009.

[28] C. Comi, A. Corigliano, G. Langfelder, A. Longoni, A. Tocchio, and B. Simoni, "A resonant microaccelerometer with high sensitivity operating in an oscillating circuit," *J. Microelectromech. Syst.*, vol. 19, no. 5, pp. 1140–1152, Oct. 2010.

[29] A. Tocchio, A. Caspani, G. Langfelder, A. Longoni, and E. Lasalandra, "A Pierce oscillator for MEMS resonant accelerometer with a novel low-power amplitude limiting technique," in *Proc. IEEE Int. Freq. Control Symp.*, May 2012, pp. 1–6.

[30] S. Sung, J. G. Lee, B. Lee, and T. Kang, "Design and performance test of an oscillation loop for a MEMS resonant accelerometer," *J. Micromech. Microeng.*, vol. 13, no. 2, pp. 246–253, Mar. 2003.

[31] A. A. Trusov, I. P. Prikhodko, S. A. Zotov, and A. M. Shkel, "High-Q and wide dynamic range inertial MEMS for north-finding and tracking applications," in *Proc. IEEE/ION PLANS*, Apr. 2012, pp. 247–251.

[32] A. A. Trusov, S. A. Zotov, B. R. Simon, and A. M. Shkel, "Silicon accelerometer with differential frequency modulation and continuous self-calibration," in *Proc. IEEE MEMS*, Jan. 2013, pp. 29–32.

[33] D. W. Burns and R. H. Frische, "Mechanical resonance, silicon accelerometer," U.S. Patent 5 780 742, Jul. 14, 1998.

[34] S.-W. Yoon, S. Pinel, and J. Laskar, "High-performance 2-GHz CMOS LC VCO with high-Q embedded inductors using wiring metal layer in a package," *IEEE Trans. Advance. Packag.*, vol. 29, no. 3, pp. 639–646, Aug. 2006.

[35] S.-H. Tseng, Y.-J. Hung, Y.-Z. Juang, and M. S.-C. Lu, "A 5.8-GHz VCO with CMOS-compatible MEMS inductors," *Sens. Actuators A, Phys.*, vol. 139, nos. 1–2, pp. 187–193, Sep. 2007.

[36] C.-L. Dai, F.-Y. Xiao, Y.-Z. Juang, and C.-F. Chiu, "An approach to fabricating microstructures that incorporate circuits using a post-CMOS process," *J. Micromech. Microeng.*, vol. 15, no. 1, pp. 98–103, Jan. 2005.

[37] H. Luo, G. Zhang, R. C. Carley, and G. K. Fedder, "A post-CMOS micromachined lateral accelerometer," *J. Microelectromech. Syst.*, vol. 11, no. 3, pp. 188–195, Jun. 2002.

[38] C. Lu, M. Lemkin, and B. E. Boser, "A monolithic surface micromachined accelerometer with digital output," *IEEE J. Solid-State Circuits*, vol. 30, no. 12, pp. 1367–1373, Dec. 1995.

[39] B. V. Amini and F. Ayazi, "A 2.5-V 14-bit $\Sigma\Delta$ CMOS SOI capacitive accelerometer," *IEEE J. Solid-State Circuits*, vol. 39, no. 12, pp. 2467–2476, Dec. 2004.

[40] P. Zwahlen, Y. Dong, A.-M. Nguyen, F. Rudolf, J.-M. Stauffer, P. Ullah, and V. Ragot, "Breakthrough in high performance inertial navigation grade Sigma-Delta MEMS accelerometer," in *Proc. IEEE/ION PLANS*, Apr. 2012, pp. 15–19.

[41] *IEEE Standard Specification Format Guide and Test Procedure for Linear, Single-Axis, Pendulous, Analog Torque Balance Accelerometer*, IEEE Standard 337, 1972.

[42] *IEEE Standard Definitions of Physical Quantities for Fundamental Frequency and Time Metrology—Random Instabilities*, IEEE Standard 1139-1999, 1999.

[43] (Accessed: 2013, Jul. 1). *Allan_Overlap* [Online]. Available: http://www.mathworks.com/matlabcentral/fileexchange/26441-allanoverlap

Yi Chiu received the B.S. degree in electrical engineering from National Taiwan University, Taipei, Taiwan, in 1988 and the M.S. and Ph.D. degrees in electrical and computer engineering from Carnegie Mellon University, Pittsburgh, PA, USA, in 1991 and 1996, respectively. From 1998 to 2001, Dr. Chiu was with Acer Media Technology (now BenQ Materials) and worked on advanced optical storage media. He is currently an Associate Professor in the Department of Electrical and Computer Engineering, National Chiao Tung University, Hsinchu, Taiwan. His research interests include energy harvesting, optical MEMS, and CMOS-MEMS sensors.

Hao-Chiao Hong (S'98–M'04–SM'12) received the B.S., M.S., and Ph.D. degrees in electrical engineering from National Tsing Hua University, Hsinchu, Taiwan, in 1990, 1992, and 2003, respectively. From 1997 to 2001, he was with Taiwan Semiconductor Manufacturing Company (TSMC), where he developed mixed-signal IPs for customers and process vehicles. He joined Intellectual Property Library Company, Hsinchu, Taiwan, as the Senior Manager of the Analog IP Department in August 2001. He has been with National Chiao Tung University, Hsinchu, Taiwan, since February 2004, where he is currently a Full Professor in the Electrical and Computer Engineering Department.

His main research interests include design for testability, built-in self-test, and calibration techniques for mixed-signal circuits and high performance mixed-signal IC design. He received the Best Paper Award from the 2009 International Symposium on VLSI Design, Automation & Test (VLSI-DAT).

Dr. Hong served as the Executive Secretary of the Mixed-signal and RF Consortium of the Ministry of Education, Taiwan, from 2006 to 2008, and the Executive Secretary of the Heterogeneous Integration Consortium of the Ministry of Education, Taiwan, from 2008 to 2009. He was the General Chair of the Sixth VLSI Test Technology Workshop (VTTW) in 2012 and the Program Chair of the Fifth VTTW in 2011. He is a Life Member of the Taiwan IC Design Association and the VLSI Test Technology Forum (VTTF), Taiwan.

Po-Chih Wu was born in Changhwa, Taiwan, in 1987. He received the B.S. degree from the Department of Electrical Engineering, National Chung Cheng University, Chiayi, Taiwan, in 2009 and the master's degree from the Institute of Electrical Control Engineering, National Chiao Tung University, Hsinchu, Taiwan, in 2013. His major research interests include CMOS MEMS capacitive accelerometers and sensor interface circuits.